Original Article

Exploring the Profiles of ROS1 Tyrosine Kinase: A Structural Analysis of G2032R and D2033N Mutations

Abstract

Background: ROS1, a proto-oncogene, drives cancer through chromosomal fusions. The G2032R and D2033N mutations, common in ROS1-rearranged non-small cell lung cancer, hinder crizotinib treatment. We investigate these mutations' impact on ROS1 structure through molecular dynamics (MD) simulations, revealing destabilization. Our findings shed light on how these mutations contribute to cancer development. **Materials and Methods:** The crystal structure of human ROS1 (PDB ID: 7z5x) served as the template for homology modeling and further mutation insertion of G2032R and D2033N substitutions introduced using Swiss-PdbViewer. The MD simulations were conducted on the wild-type (WT) and mutant ROS1 kinase domains to explore the structural changes and interactions. **Results:** The initial model of the human ROS1 crystal structure was constructed, incorporating missing loop residues and then utilized for the MD simulation studies. The examination of conformational changes in WT, G2032R, and D2033N mutant ROS1 proteins involved observing alterations in the C-alpha protein. We observed that the mutations resulted in deviations in the MD trajectory over the 500 ns period. Consequently, the MD simulations unveiled significant conformational changes induced by the G2032R and D2033N mutations, affecting protein stability and dynamics, particularly in regions such as the ATP binding and active sites. **Conclusion:** Our study constructed an initial model of the human ROS1 and used it for MD simulation studies to examine the conformational changes in ROS1 mutants. Notably, our observations revealed that the mutations caused deviations in the MD trajectory. The G2032R and D2033N mutations significantly alter ROS1 structure, affecting its stability and dynamics, offering key insights into their role in cancer disease development.

Keywords: *Molecular dynamics simulation, mutation G2032R D2033N, non-small cell lung cancer, ROS1*

Syed Ikramul Hasan

Department of Basic Medical Science, College of Applied Medical Sciences, Al-Baha University, Al Bahah, Saudi Arabia

Introduction

Lung cancer is among the deadliest malignancies worldwide, with a mortality rate exceeding that of colon, breast, and pancreatic cancers combined.[1,2] Non-small cell lung cancer (NSCLC) is a type of lung cancer that constitutes the majority (approximately 85%) of all lung cancer cases.[3,4] It originates in the tissues of the lung and is distinct from small cell lung cancer (SCLC), another main type of lung cancer.[5-7] NSCLC encompasses several subtypes, including adenocarcinoma, squamous cell carcinoma, and large cell carcinoma, each with unique characteristics.[8,9] The ROS1 gene, a proto-oncogene, encodes for the ROS1 protein, which belongs to the family of receptor tyrosine kinases.[10,11] Under normal circumstances, ROS1 is involved in essential cellular processes and signal transduction.[12] However, genetic alterations in the ROS1 gene, such as mutations or fusions, can lead to its constitutive activation, turning it into an oncogenic driver.[13-15] Cancer is a major contributor to global mortality, with nearly 10 million deaths recorded in 2020 according to the World Health Organization (WHO). Among the most commonly diagnosed cancers in 2020 were breast (2.26 million cases), lung (2.21 million cases), colon and rectum (1.93 million cases), prostate (1.41 million cases), non-melanoma skin (1.20 million cases), and stomach cancers (1.09 million cases) (WHO, 2020).[16,17]

In a subset of NSCLC cases, ROS1 alterations, including gene fusions and mutations like G2032R and D2033N, have been identified.[18-21] These alterations result in abnormal ROS1 signaling, contributing

This is an open access journal, and articles are distributed under the terms of the Creative Commons Attribution-NonCommercial-ShareAlike 4.0 License, which allows others to remix, tweak, and build upon the work non-commercially, as long as appropriate credit is given and the new creations are licensed under the identical terms.

For reprints contact: WKHLRPMedknow_reprints@wolterskluwer.com

How to cite this article: Hasan SI. Exploring the profiles of ROS1 tyrosine kinase: A structural analysis of G2032R and D2033N mutations. Int J App Basic Med Res 2025;15:4-10.

Submitted: 27-Jan-2024
Revised: 17-Apr-2024
Accepted: 02-Sep-2024
Published: 09-Jan-2025

Address for correspondence:
Dr. Syed Ikramul Hasan, Department of Basic Medical Science, College of Applied Medical Sciences, Al-Baha University, Al Bahah, Saudi Arabia.
E-mail: sshamim@bu.edu.sa

Access this article online

Website: https://journals.lww.com/IJAB

DOI: 10.4103/ijabmr.ijabmr_43_24

Quick Response Code:

to the initiation and progression of NSCLC.[22] When ROS1 is aberrantly activated in NSCLC, it stimulates oncogenic signaling pathways that promote uncontrolled cell growth and proliferation.[12,15] This unregulated cellular activity is a hallmark of cancer progression. Due to the specific role of ROS1 alterations in NSCLC, targeted therapies have been developed to address these oncogenic effects. Tyrosine kinase inhibitors (TKIs), such as Crizotinib, have shown efficacy in inhibiting the constitutive activity of the ROS1 kinase domain, providing a targeted approach for treating ROS1-positive NSCLC.[15,23-25]

In this investigation, we comprehensively analyze root mean square deviation (RMSD), root mean square fluctuation (RMSF), radius of gyration (Rg), solvent-accessible surface area (SASA) and conformational dynamics, free energy landscape (FEL), molecular motions, and configurational frustration in both wild-type (WT) and mutant ROS1 structures using molecular dynamics (MD) simulation. The G2032R and D2033N mutations induce notable alterations in C-alpha orientation, compactness, residual fluctuation, and solvent accessibility, signifying an overall destabilization of the protein structure. The essential dynamics, conformational magnitude, direction of motion, and frustration analyses further support the observation of structural loss in ROS1 due to these mutations. FEL analysis reveals a single well-defined minimum in the case of WT, while multiple wells define free energy minima in G2032R and D2033N, strongly suggesting reduced stability of ROS1 due to the mutations. This study provides insights into the molecular basis of G2032R and D2033N mutant-mediated cancer development.

Materials and Methods

Hardware and software

The hardware setup includes a Dell workstation featuring 128 GB of RAM and an NVIDIA GeForce RTX 3070 graphics card with 8 GB DDR6 memory. GROMACS is utilized for MD simulations, and Xmgrace is chosen for its superior data visualization and graph plotting capabilities.[26,27] Molecular visualization of ROS1 protein structure image generation is carried out using PyMOL.[28,29]

Homology modeling and mutation insertion

The human ROS1 protein's crystal structure (PDB ID: 7z5x) was taken from the protein data bank (PDB) and used as the template of the starting model for simulations.[30,31] The reconstruction of missing loop residues (2101-2123) was conducted using the Swiss Model server, and the modeling process was facilitated through SWISS-MODEL.[32] The ROS1 protein structure (PDB ID: 7z5x) was examined for detrimental mutations, and their locations were pinpointed within the structure. Mutant was created by substituting residues G2032R and D2033N using Swiss-PdbViewer.[33]

Molecular dynamics simulations

The ROS1 kinase domain structure was initially modeled and mutations, including G2032R and D2033N, was chosen to investigate their potential impact on the functionality of ROS1 kinase domains, encompassing modifications in structure, stability, dynamics, and interactions. Subsequently, MD simulations were conducted on both the WT and mutant (G2032R and D2033N) ROS1 kinase domains to explore the local conformational space.[34] The kinase domains were solvated with TIP3 water at 300 K and 1 atmosphere pressure, employing a simulation cell with a minimum distance of 5 angstroms in all the directions from the protein.[35] Electrostatic interactions were computed using the particle mesh Ewald simulation method, employing a short-range electrostatic cutoff of 10 angstroms.[36] A similar 10-angstrom cutoff was applied for Van der Waals interactions during the simulation.[37] The system underwent an initial energy minimization using steepest-decent and conjugate gradient algorithms over 5,000 steps. Subsequently, solvent and ions underwent equilibration for 100 ps within constant pressure (Number of particles [N], Pressure [P], and Temperature [T] [NPT]) ensembles with the protein substrates harmonically restrained using a force constant of 1,000 kJ mol^{-1} nm^{-2}. Finally, both the WT and mutant systems (G2032R and D2033N) underwent a 500 ns MD simulation.

The RMSD in GROMACS is calculated using the following equation:

$$RMSD = \sqrt{\frac{1}{N}\sum_{i=1}^{N} w_i \cdot |\, \mathrm{r}_i - \mathrm{r}_i^0 \,|^2}$$

- N is the total number of atoms or residues
- wi is an optional weight for each atom or residue
- ri is the instantaneous position vector of atom or residue
- r_i^0 is the reference position vector of atom or residue.

This equation calculates the RMSD, which measures the average deviation of atomic or residue positions between the simulated structure and a reference structure (usually the initial or a target structure) over a trajectory. The summation is over all atoms or residues, and the result is the square root of the average of the squared deviations, providing a measure of structural deviation.

Similarly, the RMSF in GROMACS is calculated using the following equation:

$$RMSF_i = \sqrt{\frac{1}{N}\sum_{j=1}^{N} \left\langle (\delta x_{ij})^2 \right\rangle}$$

Where:

- N is the total number of atoms or residues
- δxij is the deviation of the position of atom or residue i along the trajectory from its average position
- The average ⟨⟩⟨⟩ is taken over the trajectory.

This equation computes the RMSF for each atom or residue, representing the average fluctuation or mobility

of each position during the simulation. RMSF provides insights into the flexibility or stability of specific regions within a biomolecular system.

Essential dynamics

To gain a more profound understanding of the collective atomic dynamics of WT-ROS1 and its variants G2032R and D2033N, Principal Component Analysis (PCA) or essential dynamics was conducted using the GROMACS software.[38,39] The computation of eigenvectors and eigenvalues, along with the projection along the first PC1 and PC2, adhered to the established protocols. Atomic coordinates extracted from trajectories were scrutinized to generate a covariance matrix, elucidating the amplitude of dynamic motions. The atomic motions corresponding to each set of eigenvalues delineate the direction of protein dynamics. The dynamic motions of WT-ROS1, G2032R, and D2033N throughout the trajectories were computed by plotting the highest amplitude of atomic motions represented in the first two eigenvalues. PCA within GROMACS offers insights into the predominant motions within a molecular system, facilitating comprehension of conformational changes and dynamics.

Results

The SWISS-MODEL is a web-based integrated platform specifically designed for homology modeling of protein structures. Considering the deficient amino acid information in the ROS1 protein structure, we retrieved the crystal structure of human ROS1 from the PDB ID: 7z5x to serve as a template for constructing the initial models used in the simulation. Missing loop residues 2101–2123 were reconstructed through the Swiss Model server. The modeled loop region is depicted as an orange surface view [Figure 1a]. The ROS1 structure displays mutations at positions G2032R and D2033N.

The mutations were created with in the model structure, and Swiss-PdbViewer was used to change the protein amino acids to reflect the mutations [Figure 1b]. The mutant structure underwent optimization and energy minimization employing the GROMACS force field. Three distinct simulations were conducted, encompassing the WT and two mutated models.

Single amino acid substitutions in proteins can exert profound effects on their stability, folding kinetics, and physiological functions. We focus to understand the impact of ROS1 mutations, G2032R and D2033N, associated with cancer.

The investigation aims to understand how both normal (WT) and changed (mutant) ROS1 proteins behave over time, focusing on how their shapes change. Our findings reveal notable distinctions in the conformational dynamics between the WT and mutant ROS1 proteins. Specifically, the G2032R and D2033N mutations induce discernible changes in the structural behavior, indicating potential implications for the physiological functions of ROS1 in the context of cancer.

We perform MD simulations to understand structural dynamics, specifically focusing on assessing C-α structure RMSD and compactness. The structural differences between WT and mutant variants were studied using 500 ns MD simulations. The substitution of the polar uncharged glutamine at the G2032R position with a nonpolar, aliphatic Glu to form the mutate Arg with characteristics of being basic, polar, and positively charged not only influences the protein's charge potential but also induces considerable conformational changes in its structure. Furthermore, the D2033N mutation, involving the acidic, negatively charged Asp mutated to the polar and hydrophilic Asn, also has discernible effects on the structural and functional aspects of the ROS1 protein.

The examination of the conformational changes in WT and mutant ROS1 proteins involved the observation of alterations in the C-alpha protein. Initially, all systems underwent equilibration during the initial 50 ns of MD simulation. The RMSD analysis revealed an initial rise in RMSD during the early stage of simulation, reaching a peak around 150 ns. Specifically, for the G2032R mutation, the RMSD trajectory increased steadily from 50 ns to 120 ns and experienced a slight dip at 372 ns, followed by a minimal increase in motion in the trajectory from 375 to 500 ns in the MD simulation. Similarly, in case of the D2033N mutation, a substantial deviation was observed at 200 ns, 300 ns, and 400 ns of the MD simulation [Figure 2a]. The computed average RMSD

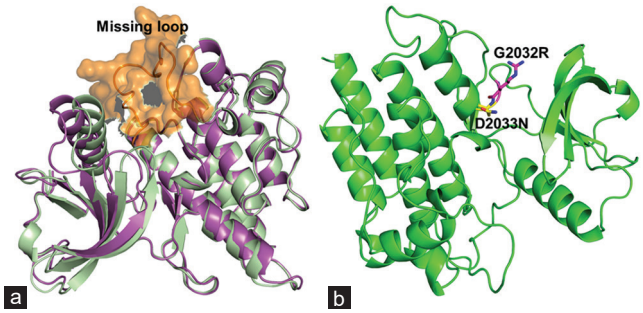

Figure 1: A comparison of the missing loop of ROS1 in the crystal structure with the modeled structure is shown in (a), with the modeled loop depicted as an orange surface view. The mutation positions G2032R and D2033N in the mutant ROS1 structure are highlighted in (b)

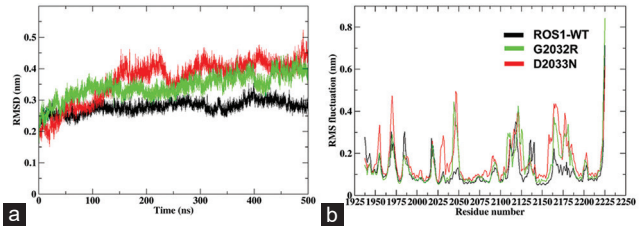

Figure 2: Molecular dynamics simulation was conducted for both the native ROS1 in the crystal structure and the mutant structure with mutations at positions G2032R and D2033N. Analysis included a root-mean-square deviation plot (a) and a root-mean-square fluctuations plot (b). Different curves in the figures are denoted by distinct colors. WT: Wild-type

values for ROS1-WT, G2032R, and D2033N were 0.277 nm, 0.364 nm, and 0.343 nm, respectively [Table 1]. This observation distinctly indicates a nonsignificant alteration in protein conformation because of the mutation.

For in-depth insights, we conducted an analysis of the residual fluctuation of each amino acid in both the WT and mutant structures of ROS1. We have examined the RMSF profiles for both the WT and the G2032R and D2033N mutants. The fluctuation values for each residue were analyzed throughout the simulation. The substitution of glycine with arginine and aspartic acid with asparagine-induced changes in the overall fluctuation pattern of ROS1 residues. The alterations in ROS1 fluctuation are particularly notable in the ATP binding site and the active site region. The structural analysis of G2032R revealed increased amino acid fluctuation, with residues at positions 2044-2048 exhibiting over 4.2 nm fluctuation, 2117-2122 displaying around 4 nm fluctuation, 2163-2169 showcasing a 4.9 nm fluctuation, and amino acid 2224-2226 demonstrating variability [Figure 2b]. Similarly, the D2033N mutation influences the fluctuation of amino acids in various regions of the protein, including 1954–1955 with a 3 nm fluctuation, 1969–1971 exhibiting over 4 nm fluctuation, 2046–2047 displaying a 4.9 nm fluctuation, 2163–2168 showed a 4.9 nm fluctuation, and 2176–2178 demonstrating around a 3.5 nm fluctuation [Figure 2b].

SASA results obtained and calculated the surface area of a biomolecule that is accessible to solvent molecules. It quantifies the extent to which a molecule's surface is exposed to the surrounding solvent. SASA values are computed as part of its analysis, providing insights into the molecular interactions and dynamics of the system under investigation. The WT and mutant structures underwent analysis of SASA, focusing on the core hydrophobic regions of both systems. A notable change in SASA was observed. The ROS1-WT, G2032R, and D2033N exhibited substantial fluctuations in SASA values 163.193, 162.405 nm², and 162.176 nm², respectively. The SASA analysis on mutants demonstrated various changes compared to WT, with the value distinguishing at 163.193 nm² [Figure 3a]. The fluctuations seen in the SASA results confirm a notable decrease in the hydrophobic connections between ROS1 protein residues due to the amino acid change.

Table 1: The ROS1-wild-type, G2032R, and D2033N were assessed for average root mean square deviation, solvent-accessible surface area, and radius of gyration values

	Average RMSD (nm)	Average SASA (nm²)	Average Rg (nm)
ROS1-WT	0.277	163.193	1.88
G2032R	0.364	162.405	1.91
D2033N	0.343	162.176	1.86

RMSD: Root mean square deviation; SASA: Solvent-accessible surface area; Rg: Radius of gyration; WT: Wild-type

The Rg results represent a metric for assessing the compactness or dispersion of a biomolecular structure throughout a MD simulation. Calculated as the root mean square distance of a group of atoms from their shared center of mass, Rg provides insights into the structural behavior of the protein. Our investigation into compactness included both the WT and mutant structures. The compactness offers information on structural tightness, which is associated with protein stability. Throughout the simulation, a slight reduction in the Rg was observed in the mutant compared to the WT. Specifically, the average Rg values for G2032R and D2033N were 1.91 nm and 1.86 nm, respectively, in contrast to the ROS1-WT Rg of 1.88 nm. The Rg results demonstrate that the G2032R mutation does not lead to a significant change in compactness; however, there is a notable loss of compactness in the case of D2033N [Figure 3b]. In total, the G2032R mutation does not induce a substantial alteration in the C-alpha protein conformation and overall compactness of the protein.

Comparing the residual displacement between the WT and mutants revealed the molecular deformation in the ROS1 protein structure. In addition, changes in the FEL of ROS1-WT, G2032R, and D2033N were investigated through MD simulations using FEL analysis, as depicted by eigenvector plots. Comparative analyses revealed the existence of stable global free energy minima concentrated within a single basin in the WT. In contrast, mutants, such as G2032R and D2033N, exhibited broader basins encompassing diverse conformations characterized by multiple metastable conformations linked to various energy minima [Figure 4a-c]. By observing, it was clear that mutations made ROS1 less stable, affecting how the protein moves. Mutants folded differently, showing unstable shapes with changed energy levels. This caused ROS1 to unfold and lose its stability.

Essential dynamics analysis was performed to know the protein accomplishes its function by collective atomic motions; therefore, it can be used to describe the important functions, including their folding, stability, and specific function. We used PCA to study how ROS1-WT, G2032R,

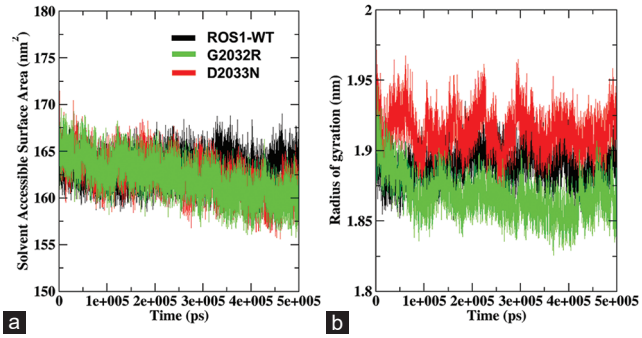

Figure 3: Molecular dynamics simulation results of the native ROS1 mutant structure with mutations at positions G2032R and D2033N. The analysis encompassed solvent-accessible surface area plot (a) and a radius of gyration plot (b). Various curves in the figures are distinguished by colors. WT: Wild-type

and D2033N mutants move. We focused on the main collective motions by analyzing the first mode of two eigenvectors or eigenvalues, which were used to create the graphs.

Results show that mutants occupy large conformational space along PC1 and PC2 as compared to WT. The changes in conformational space possibly arise due to the differences in their collective residual motion along both the eigenvectors. The large differences in the collective motion of both systems suggest that differences in the projection of collective motions of WT and mutant might disrupt the protein function. The observable spectral range of the ROS1-WT protein extends across a recognized cluster within the −1.5 nm to 2 nm range concerning eigenvector 1 (ev1) and the −2–1.5 nm² range for eigenvector 2 (ev2). Figure 5a clearly indicates that the G2032R cluster falls within the range of −2–2 nm² for ev1 and −3.5–3 nm² for ev2. Conversely, the D2033N mutant exhibits a cluster within the range of −3–2.5 nm² for ev1 and −5–3 nm² for ev2 [Figure 5a].

The plots of RMS Fluctuation 1 and RMS Fluctuation 2 against atom number illustrate the displacement regions of individual atoms, confirming their motion behavior. These observations primarily center on the variations in the flexibility of protein atoms within the residues. It is evident that certain atoms exhibit elevated fluctuations throughout the entire trajectory of the MD simulation. The cumulative evidence leads to the conclusion that complexes with G2032R and D2033N mutant structures exhibit heightened fluctuation behaviors compared to the WT-ROS1 protein [Figure 5b and c].

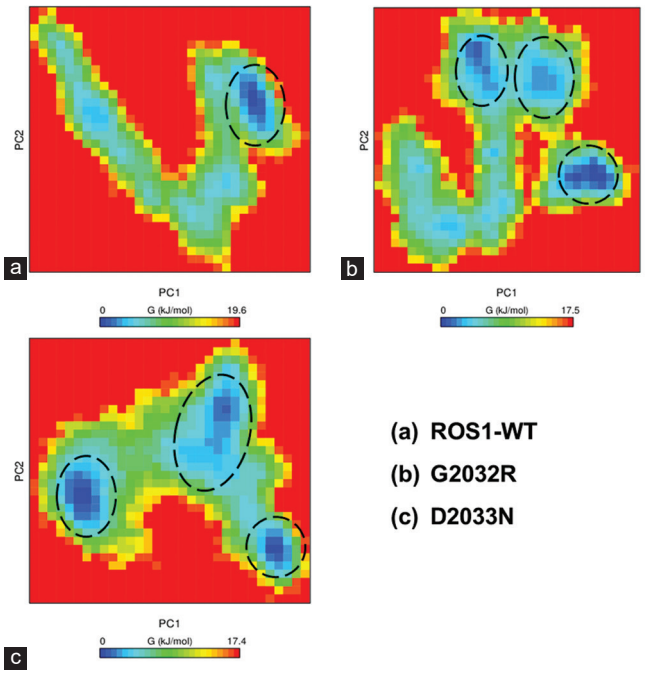

Figure 4: Free energy landscape analysis was conducted for both the wild-type ROS1 (a) and the mutant structures G2032R (b) and D2033N (c). WT: Wild-type

Additional insights into the flexibility of ROS1 mutations were gained by analyzing the temporal evolution of changes in secondary structures for G2032R and D2033N during 500 ns MD simulations, employing the define secondary structure of proteins (DSSP) program. The WT remained stable throughout the 500 ns simulation, maintaining a conserved secondary structure, while the G2032R and D2033N mutants exhibited subtle conformational fluctuations during the simulation [Figure 6a-c]. The observations revealed that in the G2032R mutant, the beta-sheet at positions 40–50 converted into a coil, the alpha helix at positions 100–120 converted to a turn, and a portion of the alpha helices at positions 150–200 converted to beta-sheet and bend structures compared to WT-ROS1. This highlights the structural disruption and coil formation in the G2032R mutation. On the other hand, alterations in secondary structural elements were noted among residues, with the beta-sheet at positions 40–50 transforming into a bend, and the alpha-helices at positions 240–260 converting into a turn and coil. The protein undergoes distortion because of the loss of helices and beta sheets.

Furthermore, the analysis of atomic density distribution also aids in comprehending alterations in atomic orientation, graphed through the utilization of the densmap script. The partial density area of the WT-ROS1 remained stable, exhibiting the minimum values of 3.56 nm^{-3}. In contrast, lower densities were observed for the mutations G2032R and D2033N, within the range of 1.98 nm^{-3} and 2.4 nm^{-3}, respectively [Figure 7]. Therefore, the analysis of density distribution confirmed

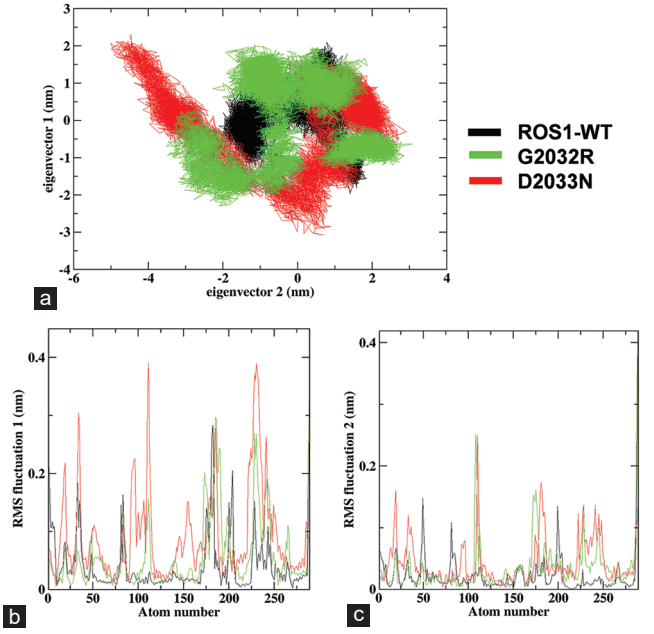

Figure 5: Two-dimensional projection plot by molecular dynamics simulation results were analyzed for ROS1 Wild-type and mutations at positions G2032R and D2033N in the mutant structure. The analysis included eigenvector 1 versus eigenvector 2 (a), root mean square (RMS) fluctuations 1 plot versus atom number for the entire system (b), and the RMS fluctuations 2 plot (c). All curves in the figures share color schemes. RMS: root mean square. WT: Wild-type

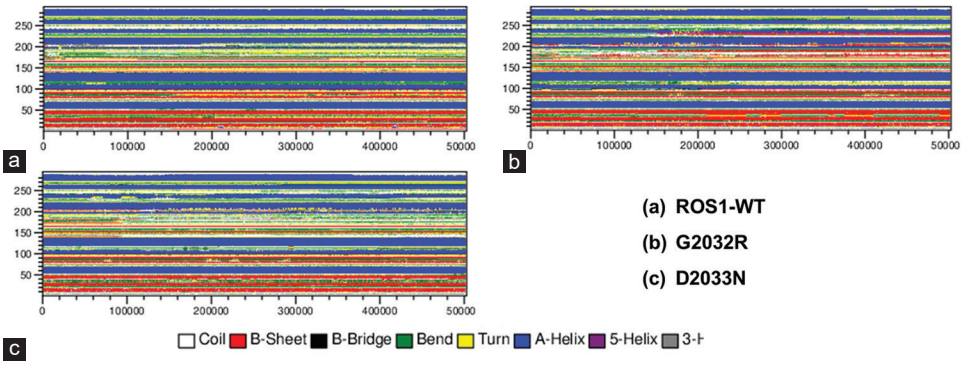

Figure 6: The graphical representation depicts alterations in the propensity of secondary structure elements, illustrating the time evolution of these elements in the protein at 300 K, classified using DSSP, for both the wild-type ROS1 (a) and the mutant structures G2032R (b) and D2033N (c). WT: Wild-type, DSSP: Define secondary structure of proteins

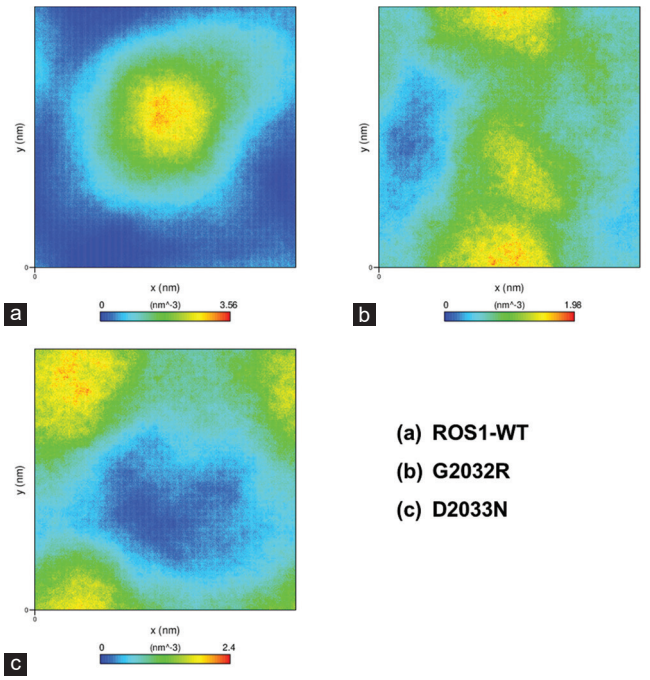

Figure 7: Density distribution analysis was graphed to comprehend atomic orientation, utilizing the densmap script for the WT and mutant structures throughout the molecular dynamics (MD) simulations. The density maps of the MD simulation trajectory analysis for ROS1 wild-type and the mutations G2032R and D2033N in the mutant structure are illustrated in panels (a-c), respectively

significant structural transitions, resulting in the destabilization on amino acid substitution.

Conclusion

ROS1 mutations, specifically G2032R and D2033N, are identified as the key contributors to resistance against crizotinib and lorlatinib. This article emphasizes the urgent need to find new types of drugs that can effectively block ROS1 mutations. The functional consequences, prevalence across diverse cancer types, and potential therapeutic targets or clinical implications associated with ROS1 (G2032R and D2033N) mutations warrant further exploration. Our investigation, utilizing MD simulation results encompassing RMSD, RG, SASA, secondary structure, and essential dynamics, reveals structural instability in the ROS1 protein. Notably, our findings affirm that the G2032R and D2033N mutations exhibit deleterious effects, severely impacting the stability of ROS1. Finally, these mutations significantly alter the conformational dynamics of the ROS1 protein, leading to functional impairment. This alteration may potentially contribute to the development of cancer, emphasizing the critical role of understanding the molecular basis of these mutations for targeted therapeutic interventions.

Ethical clearance

In the present study, no experiments involving animals were conducted. All research was performed using in silico approaches, and therefore, no ethical approval for animal studies was required.

Financial support and sponsorship

Nil.

Conflicts of interest

There are no conflicts of interest.

References

1. Zappa C, Mousa SA. Non-small cell lung cancer: Current treatment and future advances. Transl Lung Cancer Res 2016;5:288-300.
2. Kenzerki ME, Ahmadi M, Mousavi P, Ghafouri-Fard S. MYC and non-small cell lung cancer: A comprehensive review. Human Gene 2023;37:201185.
3. Gridelli C, Rossi A, Carbone DP, Guarize J, Karachaliou N, Mok T, *et al.* Non-small-cell lung cancer. Nat Rev Dis Primers 2015;1:15009.
4. Duma N, Santana-Davila R, Molina JR. Non-small cell lung cancer: Epidemiology, screening, diagnosis, and treatment. Mayo Clin Proc 2019;94:1623-40.
5. Tsoukalas N, Aravantinou-Fatorou E, Baxevanos P, Tolia M, Tsapakidis K, Galanopoulos M, *et al.* Advanced small cell lung cancer (SCLC): New challenges and new expectations. Ann Transl Med 2018;6:145.
6. Lin JJ, Langenbucher A, Gupta P, Yoda S, Fetter IJ, Rooney M, *et al.* Small cell transformation of ROS1 fusion-positive lung

cancer resistant to ROS1 inhibition. NPJ Precis Oncol 2020;4:21.
7. Lin JJ, Shaw AT. Recent advances in targeting ROS1 in lung cancer. J Thorac Oncol 2017;12:1611-25.
8. Rodak O, Peris-Díaz MD, Olbromski M, Podhorska-Okołów M, Dzięgiel P. Current landscape of non-small cell lung cancer: Epidemiology, histological classification, targeted therapies, and immunotherapy. Cancers (Basel) 2021;13:4705.
9. Socinski MA, Obasaju C, Gandara D, Hirsch FR, Bonomi P, Bunn P, *et al.* Clinicopathologic features of advanced squamous NSCLC. J Thorac Oncol 2016;11:1411-22.
10. Uguen A, De Braekeleer M. ROS1 fusions in cancer: A review. Future Oncol 2016;12:1911-28.
11. Esteban-Villarrubia J, Soto-Castillo JJ, Pozas J, San Román-Gil M, Orejana-Martín I, Torres-Jiménez J, *et al.* Tyrosine kinase receptors in oncology. Int J Mol Sci 2020;21:8529.
12. Moes-Sosnowska J, Szpechcinski A, Chorostowska-Wynimko J. Clinical significance of TP53 alterations in advanced NSCLC patients treated with EGFR, ALK and ROS1 tyrosine kinase inhibitors: An update. Tumour Biol 2024;46:S309-25.
13. Meredith DM, Cooley LD, Dubuc A, Morrissette J, Sussman RT, Nasrallah MP, *et al.* ROS1 alterations as a potential driver of gliomas in infant, pediatric, and adult patients. Mod Pathol 2023;36:100294.
14. Zhou S, Zhang F, Xu M, Zhang L, Liu Z, Yang Q, *et al.* Novel insights into molecular patterns of ROS1 fusions in a large Chinese NSCLC cohort: A multicenter study. Mol Oncol 2023;17:2200-12.
15. Iyer SR, Nusser K, Jones K, Shinde P, Keddy C, Beach CZ, *et al.* Discovery of oncogenic ROS1 missense mutations with sensitivity to tyrosine kinase inhibitors. EMBO Mol Med 2023;15:e17367.
16. Ali MA, Khan N, Ali A, Akram H, Zafar N, Imran K, *et al.* Oridonin from *Rabdosia* rubescens: An emerging potential in cancer therapy – A comprehensive review. Food Sci Nutr 2024;12:3046-67.
17. Pandit P, Shirke C, Bhatia N, Godad A, Belemkar S, Patel J, *et al.* An overview of recent findings that shed light on the connection between fat and cancer. Endocr Metab Immune Disord Drug Targets 2024;24:178-93.
18. Muminovic M, Carracedo Uribe CR, Alvarez-Pinzon A, Shan K, Raez LE. Importance of ROS1 gene fusions in non-small cell lung cancer. Cancer Drug Resist 2023;6:332-44.
19. Testa U, Castelli G, Pelosi E. ROS1-rearranged lung adenocarcinoma: From molecular genetics to target therapy. Onco 2023;3189-204.
20. Stanzione B, Del Conte A, Bertoli E, De Carlo E, Revelant A, Spina M, *et al.* Therapeutical options in ROS1-rearranged advanced non small cell lung cancer. Int J Mol Sci 2023;24:11495.
21. Sun R, Meng Y, Xu R, Li Y, Xu X, Li Z, *et al.* Construction of crizotinib resistant models with CD74-ROS1 D2033N and CD74-ROS1 S1986F point mutations to explore resistance mechanism and treatment strategy. Cell Signal 2023;101:110497.
22. Araghi M, Mannani R, Heidarnejad Maleki A, Hamidi A, Rostami S, Safa SH, *et al.* Recent advances in non-small cell lung cancer targeted therapy; an update review. Cancer Cell Int 2023;23:162.
23. Drilon A, Horan JC, Tangpeerachaikul A, Besse B, Ou SI, Gadgeel SM, *et al.* NVL-520 is a selective, TRK-sparing, and brain-penetrant inhibitor of ROS1 fusions and secondary resistance mutations. Cancer Discov 2023;13:598-615.
24. Nogami N, Nakamura A, Shiraiwa N, Kikkawa H, Emir B, Wiltshire R, *et al.* Effectiveness of crizotinib in patients with ROS1-positive non-small-cell lung cancer: Real-world evidence in Japan. Future Oncol 2023;19:2453-63.
25. Facchinetti F, Loriot Y, Kuo MS, Mahjoubi L, Lacroix L, Planchard D, *et al.* Crizotinib-resistant ROS1 mutations reveal a predictive kinase inhibitor sensitivity model for ROS1- and ALK-rearranged lung cancers. Clin Cancer Res 2016;22:5983-91.
26. Van Der Spoel D, Lindahl E, Hess B, Groenhof G, Mark AE, Berendsen HJ. GROMACS: Fast, flexible, and free. J Comput Chem 2005;26:1701-18.
27. Turner P. Center for Coastal and Land-Margin Research. Ver. 5.1.19. Vol 2. Beaverton: Oregon Graduate Institute of Science and Technology; 2005. p. 19.
28. DeLano WL. Pymol: An open-source molecular graphics tool. CCP4 Newsl Protein Crystallogr 2002;40:82-92.
29. Awad MM, Katayama R, McTigue M, Liu W, Deng YL, Brooun A, *et al.* Acquired resistance to crizotinib from a mutation in CD74-ROS1. N Engl J Med 2013;368:2395-401.
30. Petrović D, Scott JS, Bodnarchuk MS, Lorthioir O, Boyd S, Hughes GM, *et al.* Virtual screening in the cloud identifies potent and selective ROS1 kinase inhibitors. J Chem Inf Model 2022;62:3832-43.
31. Berman HM, Battistuz T, Bhat TN, Bluhm WF, Bourne PE, Burkhardt K, *et al*. The protein data bank. Acta Crystallogr D Biol Crystallogr 2002;58:899-907.
32. Schwede T, Kopp J, Guex N, Peitsch MC. SWISS-MODEL: An automated protein homology-modeling server. Nucleic Acids Res 2003;31:3381-5.
33. Guex N, Peitsch MC. SWISS-MODEL and the Swiss-PdbViewer: An environment for comparative protein modeling. Electrophoresis 1997;18:2714-23.
34. Makov G, Payne MC. Periodic boundary conditions in AB initio calculations. Phys Rev B Condens Matter 1995;51:4014-22.
35. Boonstra S, Onck PR, Giessen Ev. CHARMM TIP3P water model suppresses peptide folding by solvating the unfolded state. J Phys Chem B 2016;120:3692-8.
36. Toukmaji A, Sagui C, Board J, Darden T. Efficient particle-mesh Ewald based approach to fixed and induced dipolar interactions. J Chem Physics 2000;113:10913-27.
37. Lin IC, Seitsonen AP, Coutinho-Neto MD, Tavernelli I, Rothlisberger U. Importance of van der Waals interactions in liquid water. J Phys Chem B 2009;113:1127-31.
38. Buslaev P, Gordeliy V, Grudinin S, Gushchin I. Principal component analysis of lipid molecule conformational changes in molecular dynamics simulations. J Chem Theory Comput 2016;12:1019-28.
39. Pronk S, Páll S, Schulz R, Larsson P, Bjelkmar P, Apostolov R, *et al.* GROMACS 4.5: a high-throughput and highly parallel open source molecular simulation toolkit. Bioinformatics 2013;29:845-54.